Catalysis Letters
https://doi.org/10.1007/s10562-020-03099-x

Tuning the Basic Properties of ZnAl Hydrotalcites Modified with Ce Applied to Transesterification of Soybean Oil

Denis A. Cabrera-Munguia[1] · Horacio González[2] · Mónica Barreto-Gutiérrez[2] · Aída Gutiérrez-Alejandre[3] · José L. Rico[2] · Dora A. Solís-Casados[4]

Received: 17 September 2019 / Accepted: 4 January 2020

Abstract

The basicity of ZnAl hydrotalcite type materials was modified through the incorporation of Ce into their structure and used as heterogeneous catalysts in the transesterification of soybean oil. A series of novel ZnAl–Ce(X) catalysts was synthesized by the co-precipitation method varying the loading of Ce (X = Ce/Al molar ratio). The larger ionic radius of Ce^{3+} (1.01 Å) compared with Al^{3+} (0.53 Å) and Zn^{2+} (0.72 Å), hinders the appropriate incorporation of Ce^{3+} in the brucite-like structure, causing a small segregation of Ce^{3+} as CeO_2. However, the concentration of basic sites (acid–basic Lewis pairs) and specific surface area of the ZnAl–Ce(0.0) sample were enhanced with the incorporation of Ce, improving its catalytic activity. The most appropriate Ce loading was obtained with a Ce/Al molar ratio of 0.03, which was attributed to its large surface area, along with a higher amount of acid–basic Lewis pairs related to the presence of aluminum in pentahedral coordination. Thus, the total amount of basic sites (^{-}OH and $M–O^{-}$) of ZnAl–Ce(0.03) was triplicated, leading to a FAME yield of 80% with this catalyst, which represents an increase of 11.3% when compared with the ZnAl hydrotalcite without Ce.

Graphic Abstract

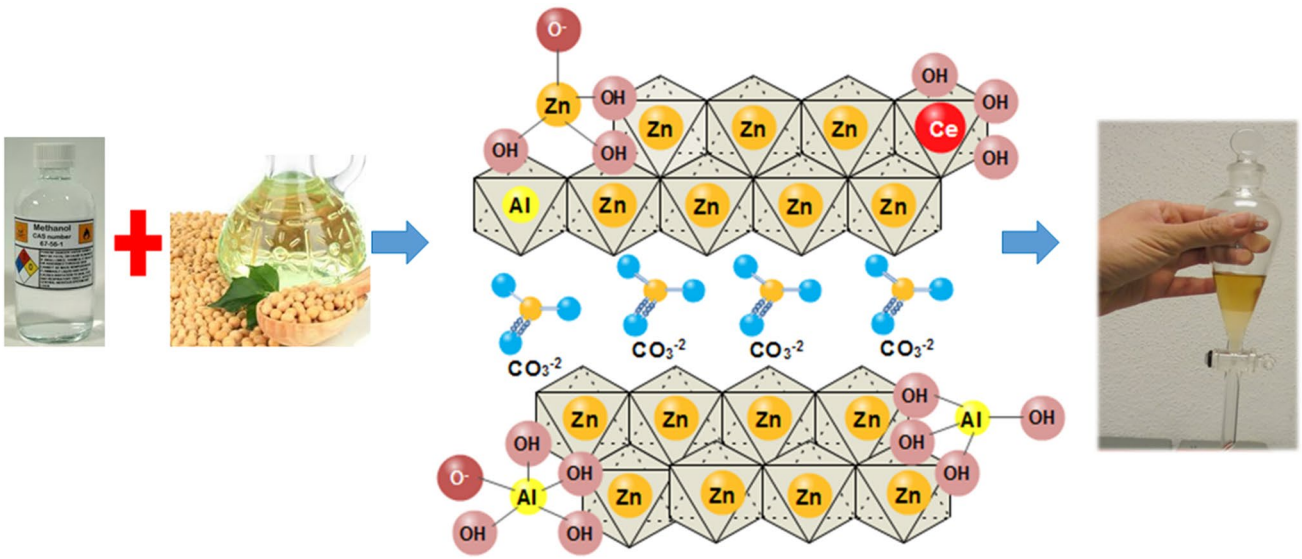

Keywords Base catalysis · Heterogeneous catalysis · Characterization · ZnAl–Ce(X) hydrotalcites · CeO_2 · Transesterification

✉ Horacio González
hogoro@umich.mx

Extended author information available on the last page of the article

Published online: 17 January 2020

1 Introduction

The growing need for new fuels able to gradually replace derivatives of petroleum, reducing at the same time the emission of pollutants, represents an important challenge [1]. An alternative to solve this problem is the use of biofuels such as bioethanol and biodiesel, whose emissions of SO_X, NO_x and short length hydrocarbons are lower when compared to their counterpart fossil fuels [2].

It is well known that biodiesel is produced effectively via transesterification of vegetable oils or animal fats on catalysts with basic properties [3, 4]. It is also widely accepted that it is desirable to use heterogeneous catalysts to avoid a high cost in the separation of the reaction products [3, 5]. Recently, studies related to the design of heterogeneous basic catalysts for transesterification reactions have focused on the achievement of high FAME yields along with the synthesis of highly stable catalysts, resistant to deactivation, leading to an economical and competitive way to produce biodiesel coming from vegetable oils and animal fats with a low content of water and free fatty acids (FFAs) [3, 4]. If it is not the case, some pretreatments are necessary to reduce the amount of water and FFAs, to avoid the poisoning of basic active sites.

Several types of heterogeneous catalysts with basic properties have been studied and reported in the literature, and can be classified into four main groups: basic zeolites [6, 7], oxides of alkaline and alkaline earth metals [8, 9], composites of transition metals [10, 11] and hydrotalcites [10, 12].

Among the desirable properties of heterogeneous basic catalysts for the transesterification reactions, stand out, a wide pore size distribution to facilitate the transport of reactants and products in the cavities of the catalysts [13] and a high concentration of basic sites to accomplish the FAME yield specification required by the EN14214. Nonetheless, the strength of the basic sites must be modulated to avoid their deactivation by the adsorption of triglycerides or free fatty acids [14].

In this sense, hydrotalcites are promising catalysts since they present a microporous–macroporous pore network along with their inherent basic nature that could be modulated using thermal treatments to obtain weak basic sites (^{-}OH), medium strength basic sites ($M–O^{-}$) and strong basic sites (O^{2-}) [15].

Hydrotalcites with general formula $[M_{1-x}{}^{2+}M_x{}^{3+}(OH)_2](A^{n-})_{x/n}{\cdot}yH_2O$ are double layered hydroxides that are commonly composed of Mg and Al as divalent and trivalent cations, respectively [16]. Novel research indicates that the substitution of Mg^{2+} by Zn^{2+} generates catalysts with better resistance to deactivation by water and free fatty acids [14, 17], but at the same time the basic properties of hydrotalcites are negatively affected. Thus, an option to overcome this problem is the incorporation of a third metal into the brucite-like structure of hydrotalcites, such as Li^{+}, Mn^{2+}, Zr^{4+}, La^{3+} or Ce^{3+} [10, 18-21]. Cerium is a rare-earth element that has been applied as a dopant in photocatalysis [22, 23], aldol condensation [20], CO_2 hydrogentation [19], CO catalytic oxidation [24], oxidation of Volatile Organic Compounds (VOC's) [21], syngas production [25] and most recently in transesterification reactions [26-28]. The dopant effect of Ce has contributed to improve the basic properties of catalysts such as CaO [29, 30], and MgAl hydrotalcites [26]. Nonetheless, just a few works have reported the synthesis of ZnAl hydrotalcites with the incorporation of Ce^{3+}, and their application was mainly focused on photocatalysis or methanol steam reforming [22, 25]. Therefore, the published research regarding the synthesis and application of ZnAl–Ce hydrotalcites to transesterification reactions of vegetable oils is scarce. In a related work MgAl–Ce hydrotalcites [26] were applied to the transesterification reactions of soybean oil, however, the effect of Ce in the doping of MgAl hydrotalcites was not clarified since the strong character of sodium aluminate, formed by pollution with sodium salts, masked the effect of Ce on their basic properties.

Thus, the aim of the present work is to obtain a deep understanding regarding the effect of the incorporation of Ce into ZnAl hydrotalcites and to analyze how the physicochemical properties (crystalline, textural, and morphological) and specially the basicity, are modified when ZnAl–Ce hydrotalcites are activated at low temperature (200 °C). The relationship between the physicochemical properties of the catalysts and their catalytic activity for the transesterification of soybean oil with methanol is also investigated, and finally the reusability of ZnAl–Ce(X) catalysts is studied during several reaction cycles.

2 Experimental

2.1 Catalysts Preparation

ZnAl–Ce(X) hydrotalcite-like materials were synthesized through the co-precipitation method, dissolving the corresponding salts of $Zn(NO_3)_2{\cdot}6H_2O$, $Al(NO_3)_3{\cdot}9H_2O$, and $Ce(NO_3)_3{\cdot}6H_2O$ in distillate water to obtain a molar ratio of Zn/Al = 2, and varying the Ce/Al molar ratio, which hereafter we will call as X, where X = 0.0, 0.01, 0.02, 0.03, 0.04 and 0.05. The pH of this solution was adjusted to 9 ± 0.5 using a Na_2CO_3–NaOH solution. The white suspension obtained was kept under reflux at 90 °C during 36 h. The precipitated was washed with deionized water and dried at 80°C during 12 h. ZnAl–Ce(X) materials were activated at

200 °C with a heating ramp of 0.5 °C/min during 6 h. This temperature was selected according to a previous work [14]. Likewise, the $Ce(NO_3)_3{\cdot}6H_2O$ salt was precipitated under the same synthesis conditions described above, hereafter called Ce precipitated precursor.

2.2 Characterization

XRD patterns of ZnAl–Ce(X) materials synthesized and activated at 200 °C were acquired in a Bruker D8 Advance equipment in a 2θ range from 5° to 80° with a Cu Kαx ray source (λ = 1.540 Å). Identification of crystalline phases was carried out using the JCPDS data base. The surface area was determined by N_2 adsorption using the BET method. Nitrogen physisorption experiments were performed in a Quantachrome Autosorb iQ instrument, the samples were previously outgassed at 200°C during 6 h. Diffuse Reflectance UV–Vis spectra of ZnAl–Ce(X) materials were obtained at room temperature from 200 to 2500 nm employing a UV–Vis–NIR spectrophotometer from Varian, Cary 500 Scan mode. Thermogravimetric analysis (TGA) was performed using a Perkin Elmer instrument in a Simultaneous Thermal Analyzer STA 6000. The simultaneous TGA–DTA analysis was carried out at a dwell of 10 °C/min from 30 to 800 °C under a helium atmosphere (40 mL/min). Scanning Electron Microscopy (SEM) was performed using a JEOL scanning electron microscope JSM-7600F in high vacuum mode, at low voltage (5 kV). The total basicity of ZnAl–Ce(X) samples was quantified by titration with benzoic acid [31] and the base strength was determined by Hammet titration [17], the Hammet indicators included Bromothymol Blue (pK = 7.2), Phenolphthalein (pK = 8.2), 2,4-Dinitroaniline (pK = 15) and 4-Nitroaniline (pK = 18.4).

^{27}Al MAS NMR spectra were acquired under MAS conditions on a Bruker Avance-III HD 400, using a probe PH-MAS 400 MHz SB 4 mm. The samples were spinning at 9 kHz, and the chemical shifts were expressed as ppm of aqueous $Al(NO_3)_3$. The X-ray photoelectron analysis (XPS) was carried out using a JEOL photoelectron spectrometer model JPS-9200 equipped with a monochromatic Mg X-ray radiation (300 W, 15 kV and 1253.4 eV). The ZnAl–Ce(X) catalysts activated at 200 °C were deposited on a conducting scotch tape and studied without any pretreatment. The samples were located in Al tapes on stainless steel sample holders, which remained in a pre-analysis chamber until a pressure of 10^{-3} mbar was achieved before entering the analysis chamber. Survey spectra were recorded from 0 to 1100 eV at constant pass energy of 100 eV, onto 900 μm^2 of analysis area; narrow spectra of C1*s*, O1*s*, Al2*p*, Zn2*p* and Ce3*d* regions were recorded in the constant pass energy mode at 20 Ev, dwell 100 and 10 scans at least. Charge correction was adjusted with carbon signal C1*s* 284 eV. Specsurf Version 1.8.2 was used for acquisition and also origin v. 8.2 for data analysis. A Shirley type background was subtracted as baseline from the spectra and the signal was deconvoluted using Gaussian curves to determine binding energies of the different element core level. NIST database was used to identify the corresponding element of the measured binding energies.

2.3 Reaction Study

A well-mixed stainless steel Parr-5000 batch reactor of 45 mL was charged with 0.3 g of catalyst, 10 g of soybean oil (molecular weight of 872.4 g/mol) and a MeOH/oil molar ratio of 30:1. The head space was purged with nitrogen during 5 min and pressurized at 20 bar to keep methanol in the liquid phase. The temperature was then rapidly increased to 200 °C, and at this condition, the stirring was set to 600 rpm. Ending the reaction time (2 h) the reactor was put in an ice bath and then depressurized. The catalyst was removed from the reaction mixture by centrifugation and the remaining methanol was eliminated by evaporation at 70 °C. Two phases were formed, the top layer was biodiesel and a small amount of glycerol at the bottom, which was separated by decantation. To remove any moisture, Na_2SO_4 was added to the product mixture and then filtrated [14]. To set the reaction temperature and MeOH/oil molar ratio, additional experiments were performed under the same conditions mentioned above, but varying the reaction temperature (140, 160, 180 and 200 °C) and MeOH/oil molar ratio (12:1, 18:1, and 30:1) using the ZnAl–Ce(0.0) material. The kinetics experiments were carried out under the experimental conditions mentioned previously, but varying the reaction time (20, 40, 60, 100, and 120 min).

The GC analysis of FAMEs was performed in a Hewlett Packard 5890 gas chromatograph equipped with a HP-2 (30 m × 0.25 mm × 0.25 μm) column. The temperature of the injector and the flame ionization detector was set at 250 °C and 300 °C, respectively. To quantify the amount of methyl ester, heptadecanoic acid of methyl ester, heptane and nitrogen were used as the internal standard, solvent and gas carrier, respectively. The FAME yield was calculated from the following equation [13]:

$$\%\, FAME\, yield = \left(n_{FAME}/3n_{TG}\right) \times 100 \quad (1)$$

where n_{TG} represents the initial mol of triglycerides, n_{FAME} the produced mol of FAME quantified by GC–MS, and 3 is the stoichiometric coefficient of the transesterification reaction. The catalytic experiments were conducted three times and the FAME yields reported are the average data with standard deviation (σ) of 1.0 to 4.5%.

The TOF evaluation for each ZnAl–Ce(X) catalyst was performed at the same reaction conditions described above using the data at 20 min. The TOF was calculated [32] according to the following equation:

$$TOF = r/f_m \quad (2)$$

where TOF is the turnover number in s^{-1}, r is the reaction rate in mmol/(s g_{cat}), and f_m is the concentration of basic sites in mmol/g_{cat}.

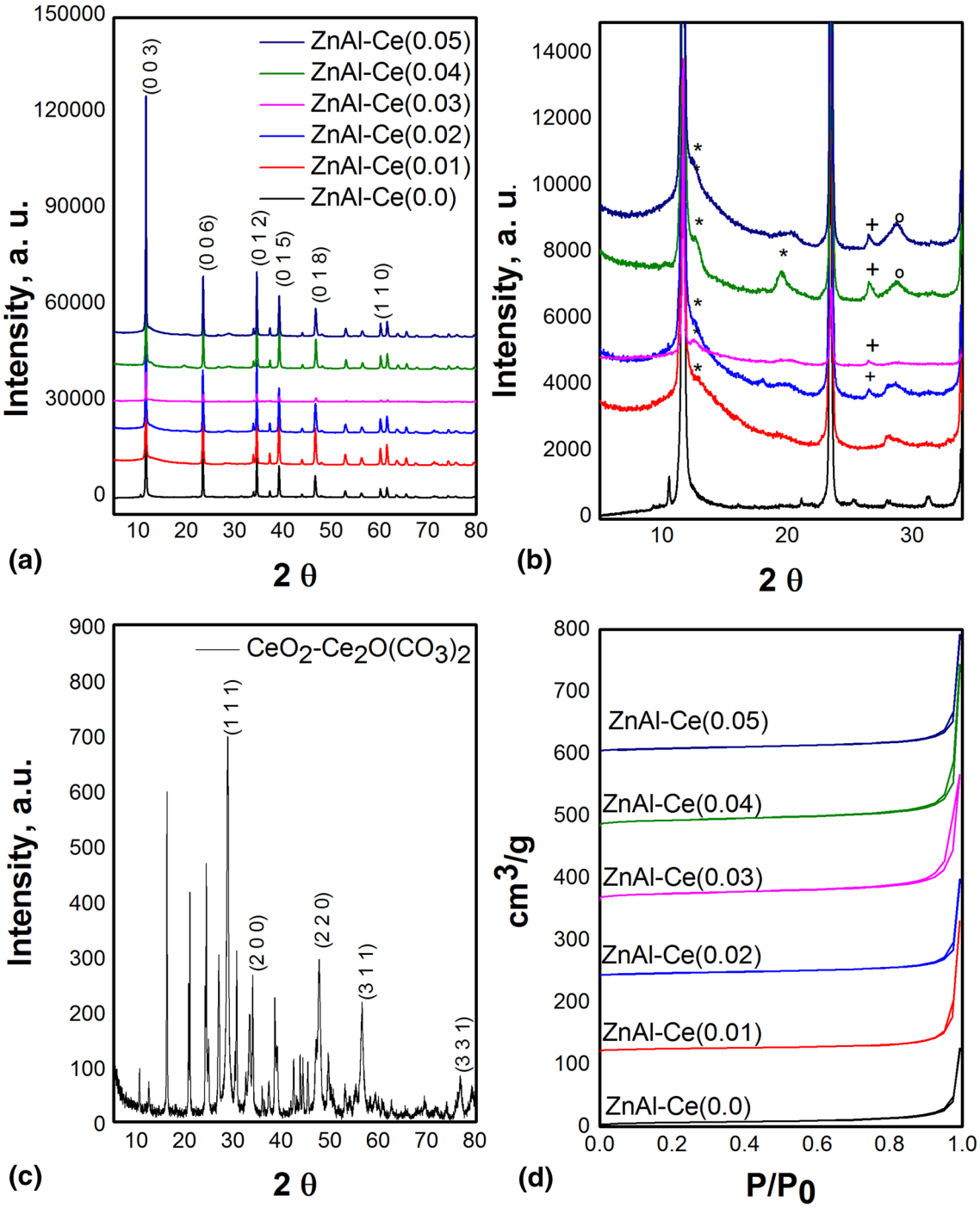

Fig. 1 **a** XRD patterns of ZnAl–Ce(X) materials at 80 °C, **b** Segregation of $*Zn_5(CO_3)(OH)_6$, + $Ce_2O(CO_3)_2$, °CeO_2 in ZnAl–Ce(X) material, **c** XRD pattern of Ce precipitated precursor, and **d** N_2 adsorption–desorption isotherms of ZnAl–Ce(X) materials

3 Results and Discussion

3.1 Characterization of the ZnAl–Ce(X) Materials

The X-ray diffractograms of ZnAl–Ce(X) materials, plotted in Fig. 1a show the typical diffraction lines attributed to ZnAl hydrotalcite-like materials at 2θ = 11.6, 23.3, 34.4, 39.1, 46.7 and 60.1 (PDF 04-011-8023), related to the (0 0 3), (0 0 6), (0 1 2), (0 1 5), (0 1 8) and (1 1 0) reflections [18, 19, 22]. A deep analysis of the XRD patterns (Fig. 1b) shows segregation of the crystalline phases hydrozincite ($Zn_5(CO_3)_2(OH)_6$, PDF 19-1458), ceria (CeO_2, PDF 34-0394) and cerium oxide carbonate ($Ce_2O(CO_3)_2$, PDF 43-0602). A small and wide band located at 2θ = 13.1° is related to hydrozincite, which becomes more prominent when the Ce/Al molar ratio increases. The appearance of hydrozincite obeys to the carbonation of ZnO that was not incorporated to the brucite-like structure [33]. In addition, the peaks at 2θ = 26.5° and 29.2° are related to $Ce_2O(CO_3)_2$ and CeO_2 [18, 34], respectively, whose intensities are more pronounced as the amount of Ce incorporated increases, which is attributed to the large ionic radius of Ce^{3+} (1.01 Å) compared with Al^{3+} (0.53 Å) and Zn^{2+} (0.72 Å), complicating the incorporation of Ce^{3+} into the hydrotalcite structure [21]. The presence of these Ce crystalline phases could be related to the low electronegativity of Ce (1.12) compared with Zn (1.65) and Al (1.61), which favors the formation of carbonate and hydroxide species in the stage of co-precipitation synthesis [20]. Moreover, the X-ray diffraction pattern of the Ce precipitated precursor (Fig. 1c) shows that $Ce(NO_3)_3 \cdot 6H_2O$ salt precipitates as a mixture of $Ce_2O(CO_3)_2$ and CeO_2, showing the main crystalline planes (111), (200), (220), (311), and (331) of CeO_2 located at 2θ = 29.2°, 33.1°, 47.5°, 57.8° and 76.7° [34].

Table 1 presents the lattice constants *a* and *c* estimated from the XRD patterns for ZnAl–Ce(X) catalysts, the lattice *a* is obtained multiplying the interplanar distance of the (110) reflection times two, and the lattice *c* is obtained multiplying the interplanar distance of the (003) reflection times three [35]. The lattice constant *a* is indicative of the average cation-cation distance in the brucite layer [20]. The values of this parameter changed very little for all ZnAl–Ce (X) catalysts, in fact the most important change of this parameter occurs for the ZnAl–Ce(0.03) catalyst which only showed a slight decrease. The *c* parameter which is related to the thickness of the brucite-like layer and the hydrotalcite interlayer distance, is also slightly decreased for ZnAl–Ce(0.03) and ZnAl–Ce(0.04) samples, which suggests an increase in the electrostatic forces of attraction between the layers and the interlayer anions of such samples. This result could be related to the larger ionic radius and low electronegativity of Ce^{3+} which replaces Al^{3+} cations, presumably due to an increase in the electrostatic attraction of the charged brucite-like layer with the interlayer [36, 37].

Table 1 Crystallographic parameters and textural properties of ZnAl–Ce(X) catalysts

Catalyst	Parameter *a* (Å)	Parameter *c* (Å)	S_{BET} (m^2/g)
ZnAl–Ce(0.0)	2.9347	22.6536	30.1
ZnAl–Ce(0.01)	2.9361	22.7271	45.2
ZnAl–Ce(0.02)	2.9351	22.7271	53.8
ZnAl–Ce(0.03)	2.9306	22.6494	71.5
ZnAl–Ce(0.04)	2.9321	22.6474	63.4
ZnAl–Ce(0.05)	2.9331	22.6872	44.5

Figure 1d exhibits N_2 physisorption isotherms (type IV) and H3 hysteresis loops for all ZnAl–Ce(X) materials, which are characteristic of aggregates of platy particles containing slip-shaped pores [16]. Table 1 also presents the values of specific surface area of ZnAl–Ce(X) samples, among which the ZnAl–Ce(0.03) catalyst presents the highest value of surface area (71.5 m^2/g), duplicating the specific surface area of the material without Ce. This result indicates that with a Ce/Al molar ratio of 0.03, the Ce^{3+} cation is adequately incorporated into the brucite-like framework, causing a distortion in its structure.

UV–Vis–DRS spectra of ZnAl–Ce(X) materials are exhibited in Fig. 2a. It can be noticed that with exception of the ZnAl–Ce(0.0) catalyst, all samples show an intense band with a maximum at ~ 300 nm whose intensity increases as the Ce/Al molar ratio also augment. The UV–Vis–DRS spectrum of the Ce precipitated precursor, plotted in Fig. 2b, shows a wide band which was deconvoluted in three bands. The bands located at 230 nm and 275 nm are related to $O^{2-} \rightarrow Ce^{3+}$ and $O^{2-} \rightarrow Ce^{4+}$ charge transfer transition between O2p and Ce4f, respectively, while the band at 325 nm is named transition band [24]. Likewise, UV–Vis–DRS spectra of ZnAl–Ce(X) materials were deconvoluted (not shown) in three bands with maxima at 250, 290, and 330 nm. The relative percentage of each band for these materials is presented in Table 2, where no appreciable differences between the relative percentages of Ce oxidation states are detected, except for the ZnAl–Ce(0.03) sample. This last catalyst shows a higher relative population of charge transfer transition between $O^{2-} \rightarrow Ce^{4+}$, and thus, a smaller population of oxygen vacancies [38] in the octahedral unit cells that contain Ce in its highest oxidation state. As oxygen vacancies in hydrotalcites are traduced as active sites [14], this implies that these "missing" oxygen vacancies must be located in the octahedral unit cells of Zn or Al.

SEM micrographs of fresh ZnAl–Ce(0.0) (Fig. 3a) and ZnAl–Ce(0.03) (Fig. 3b) catalysts, show homogeneous plate-shaped crystals of uniform sizes (50–200 nm) with a

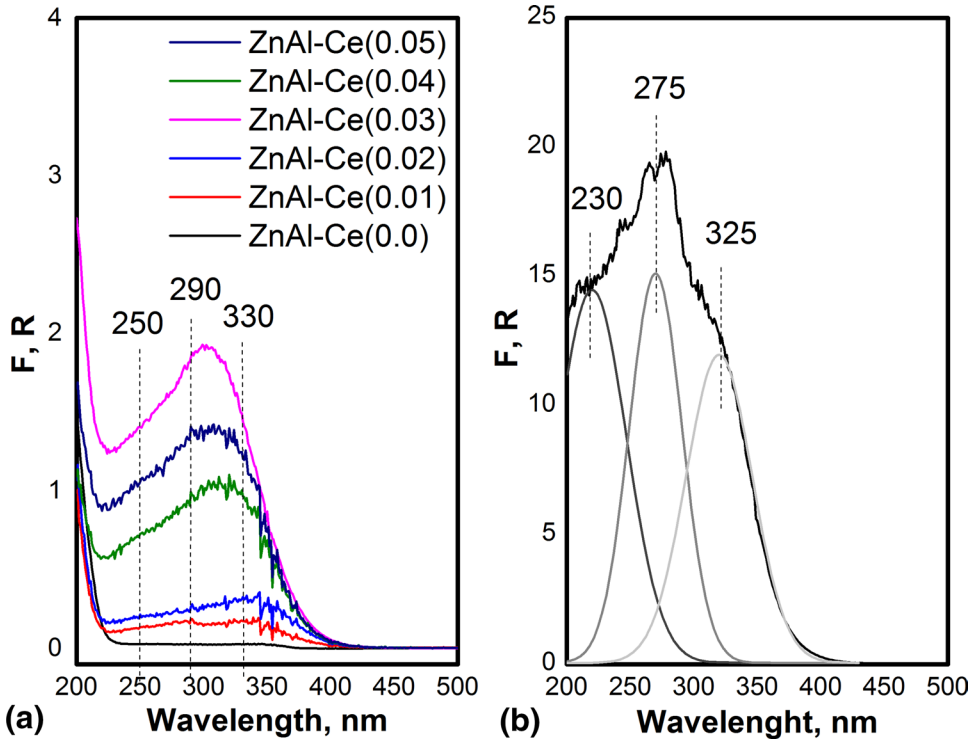

Fig. 2 **a** UV–Vis–DRS spectra of ZnAl–Ce(X), and **b** UV–Vis–DRS spectrum and deconvolution of CeO_2–$Ce_2O(CO_3)_2$

Table 2 Deconvolution of UV–Vis–DRS spectra of ZnAl–Ce(X) materials

Catalyst	Ce^{3+} (%)	Ce^{4+} (%)	Transition band (%)	Ce^{3+}/Ce^{4+}
ZnAl–Ce(0.01)	27.5	34.8	37.7	0.7898
ZnAl–Ce(0.02)	26.5	34.5	39.0	0.7702
ZnAl–Ce(0.03)	22.8	41.0	36.2	0.5552
ZnAl–Ce(0.04)	28.2	36.9	34.9	0.7669
ZnAl–Ce(0.05)	29.5	36.8	33.7	0.8009

dense stacking [19]. The platelets of ZnAl–Ce(0.0) materials are much larger than that of ZnAl–Ce(0.03), which is in line with the lower values of the cell parameters calculated for this latter material, indicating a loss of crystallinity. It is also observed that the incorporation of Ce^{3+} generates crystals studded with small grains [26].

Elemental analysis, performed by EDS, of ZnAl–Ce(0.0) and ZnAl–Ce(0.03) samples (Fig. 4), confirmed that such catalysts do not contain remaining sodium from the salts used during the co-precipitation method. Table 3 shows the

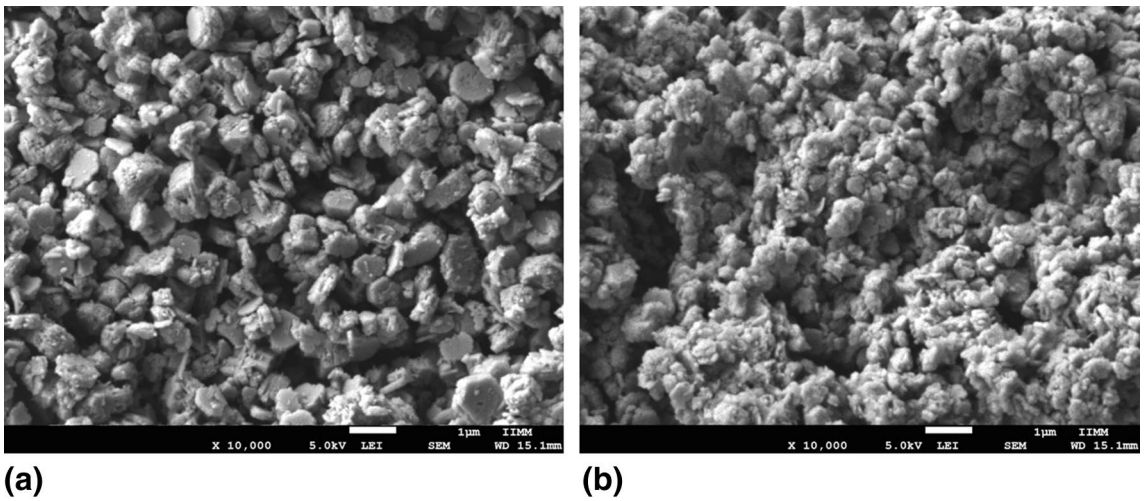

Fig. 3 SEM micrographs of **a** ZnAl–Ce(0.0), and **b** ZnAl–Ce(0.03) catalysts

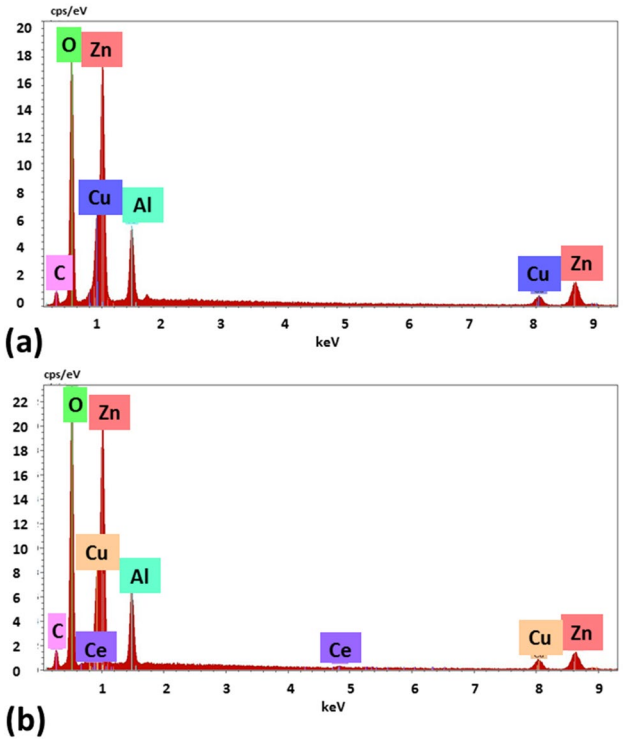

Fig. 4 EDS of **a** ZnAl–Ce(0.0), and **b** ZnAl–Ce(0.03) catalysts

Table 3 Elemental analysis of ZnAl–Ce(0.0), and ZnAl–Ce(0.03) materials

Catalyst	Zn (%)	Al (%)	Ce (%)
ZnAl–Ce(0.0)	75.76	24.24	0.0
ZnAl–Ce(0.03)	70.89	28.25	0.86

molar percentage of Zn, Al and Ce for ZnAl–Ce(0.0) and ZnAl–Ce(0.03) samples, from this information the Ce/Al molar ratio was estimated, giving a value of 0.03, which agrees well with the composition used in the preparation of the ZnAl–Ce(0.03) catalyst, indicating a successful incorporation of Ce in this sample.

Analysis of XRD patterns, N_2 physisorption isotherms and UV–Vis–DRS spectra denote that the incorporation of Ce^{3+} does not cause a significant change in the size and shape of hydrotalcite particles, resulting in ZnAl–Ce(X) materials with platelet particles, and just a small segregation of cerium as CeO_2 and $Ce_2O(CO_3)_2$, particularly when the Ce/Al molar ratio is increased.

Figure 5 shows the DTA curves of ZnAl–Ce(X) catalysts. From the DTA curve of the ZnAl–Ce(0.0) sample (Fig. 5a) three weight loss-steps are identified [39], the first one located at 208 °C, associated with the dehydration process by the loss of physisorbed and interlamellar water. The second weight loss-step, at around 262 °C, is attributed to carbonates decomposition. The last weight loss-step, located at around 395 °C, is associated with the decomposition of the hydrotalcite-like structure. Similarly, the DTA curves of ZnAl–Ce(X) samples (Fig. 5b) show the first weight loss-step at around 200 °C, it is also observed that ZnAl–Ce(0.01), ZnAl–Ce(0.02) and ZnAl–Ce(0.03) samples present the dehydration process at lower temperatures than that of ZnAl–Ce(0.0). The ZnAl–Ce(0.03) catalyst stands out by its lower temperature for water loss, located at around 188 °C. This result implies that at low temperature the accessibility to the inherent Brönsted basic sites ($^{-}$OH) of the sample is enhanced, as well as the dehydroxylation process (loss of interlamellar water) that gives rise to the formation of acid–basic Lewis pairs (M–O) [15].

The second weight loss-step of ZnAl–Ce(X) samples is located at around 280 °C without significant difference between these samples, however, in this case the decarbonation process is achieved at higher temperature when compared with the ZnAl–Ce(0.0) sample. This result is related to the strengthening of the interaction between the hydrotalcite layer and the interlayer when Ce^{3+} is incorporated [37] thus increasing its basicity. The third weight loss-step begins at around 500 °C and continues up to 900 °C [22].

3.2 Total Basicity and Catalytic Performance of ZnAl–Ce(X) Materials

In order to better understand the catalytic behavior of ZnAl–Ce(X) materials, catalytic experiments were carried out with the ZnAl–Ce(0.0) catalyst varying the reaction temperature (140, 160, 180 and 200 °C). Figure 6a shows that the catalytic activity is dramatically reduced when the reaction temperature decreases from 200 to 140 °C. This is related to the strong dependence of the kinetic constant with the reaction temperature, and also to the poor miscibility of the oily and alcoholic phases at 140 °C, which hinders the mass transport of reactive and products to the catalyst active sites, whereas at 200 °C triglycerides and methanol are completely miscible [40]. Then, reaction temperature plays a key role in the transesterification reaction since methanol must be transported to the active basic sites of the catalyst to form methoxy groups, which should be in contact with triglycerides for the transesterification reaction to proceed. Then, 200 °C is a suitable reaction temperature to perform the transesterification reaction without affecting the biodiesel quality, due to side reactions. Figure 6b shows that the catalytic activity increases as the MeOH/oil molar ratio increases, which is in line with LeChatelier's equilibrium principle. However, a MeOH/oil molar ratio of 30:1 was chosen to preserve the economy of the process and also, because a large amount of methanol hinders the separation of glycerol from biodiesel [40].

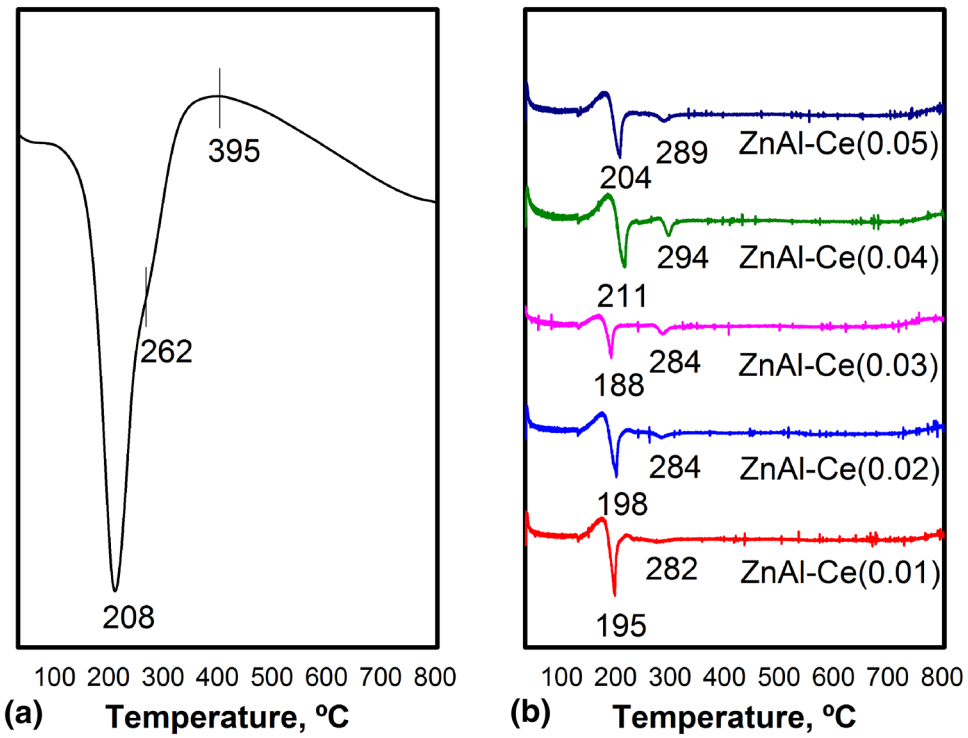

Fig. 5 **a** DTA curve of ZnAl–Ce(0.0), and **b** DTA curves of ZnAl–Ce(X) materials

A thermal treatment at 200 °C was selected to activate the ZnAl–Ce(X) samples, since as previously demonstrated [14] at this temperature ZnAl hydrotalcite-like materials exhibit high catalytic activity due to the better accessibility to Brönsted basic sites ($^{-}$OH) and the formation of acid-basic Lewis pairs (M–O^{-}). In addition, according to the DTA curves of ZnAl–Ce(X) samples, dehydration and dehydroxylation processes are favored at this temperature (200 °C).

The XRD patterns of ZnAl–Ce(X) materials activated at 200 °C (Fig. 7a), suggest the loss of water and CO_3^{2-} groups, which is evident from the decreased intensity of the typical peaks of the hydrotalcite. However, these diffraction signals are more defined and intense for the ZnAl–Ce(0.03) catalyst, which is attributed to its stronger basic sites due to a higher retention of CO_3^{2-} groups. In addition, all ZnAl–Ce(X) samples show a broadband at $30° < 2\theta < 40°$ indicating the presence of the zincite phase (ZnO, PDF 01-089-1397) which has been previously related to the high catalytic activity in the transesterification of vegetable oils [12]. Hydrozincite ($Zn_5(CO_3)_2(OH)_6$, PDF 19-1458), the precursor of zincite, is also identified as a small peak at $2\theta = 20°$ in ZnAl–Ce(0.03) and ZnAl–Ce(0.04) samples, this crystalline phase is formed when the hydrotalcite is heated up to 200 °C and then, partially decomposed to ZnO [41].

A diffraction peak assigned to $ZnCO_3$ (PDF 03-0774) was also observed at $2\theta = 25.5°$ in the ZnAl–Ce(0.0) sample, denoting a partial segregation of this material during thermal activation. In the case of ZnAl–Ce(X) samples, diffraction peaks at $2\theta = 29.2$, 47.5 and 57.6° indicate segregation of CeO_2 (PDF 34-0394), whose intensity increases when the Ce/Al molar ratio augments.

The results of total basicity of ZnAl–Ce(X) samples activated at 200 °C (Table 4) indicate that the incorporation of Ce to the ZnAl hydrotalcite, increases the concentration of basic sites in relation to the material without Ce. This result is more evident for the catalyst containing a Ce/Al molar ratio of 0.03 for which the total basicity is practically triplicated.

According to the results presented in Table 4, the total basicity of the Ce precipitated precursor possesses basic sites of lower strength than the ZnAl–Ce(X) samples. Thus, the lower basicity of ZnAl–Ce(0.04) and ZnAl–Ce(0.05) catalysts is explained by the segregation of CeO_2 caused by Ce that was not incorporated into the brucite-like framework. These results are in line with the TOF values calculated from Eq. (2) using a reaction time of 20 min. As it is observed in Table 4, the TOF values of ZnAl–Ce(X) materials with Ce/Al molar ratios (X) of 0.01, 0.02 and 0.03 are higher than the one corresponding to the ZnAl–Ce(0.0) catalyst in 15, 25 and 40%, respectively. Indicating that the incorporation of Ce into the ZnAl hydrotalcite framework enhances the number of molecules of triglycerides that can be converted into FAME per catalytic site of ZnAl–Ce(X) catalysts and per unit time.

Figure 7b shows that FAME yields obtained with ZnAl–Ce(X) catalysts are in line with their concentration of basic sites. Hence, the FAME yield obtained with the

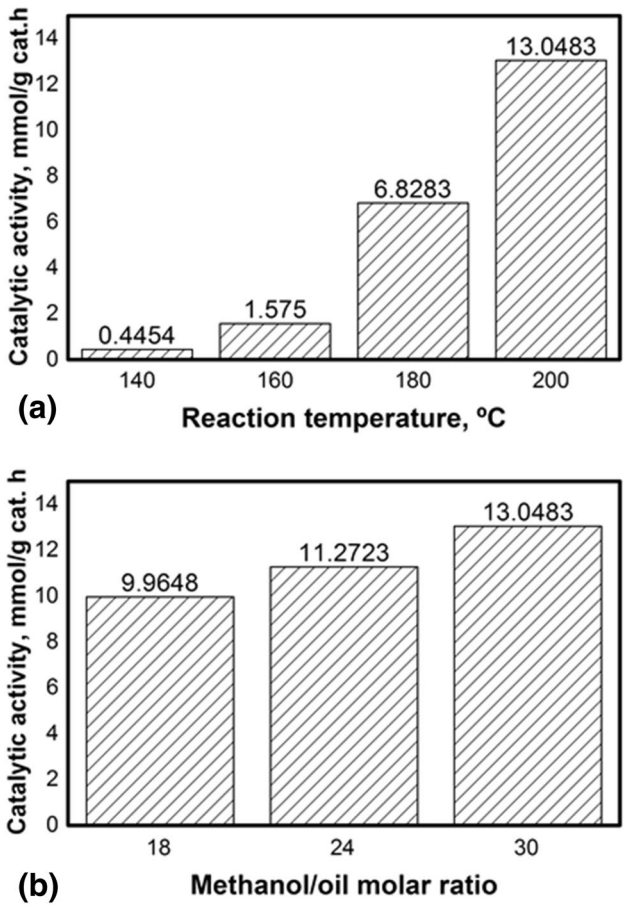

Fig. 6 Effect of: **a** reaction temperature and **b** MeOH/oil molar ratio on the catalytic activity of ZnAl–Ce(0.0) catalyst

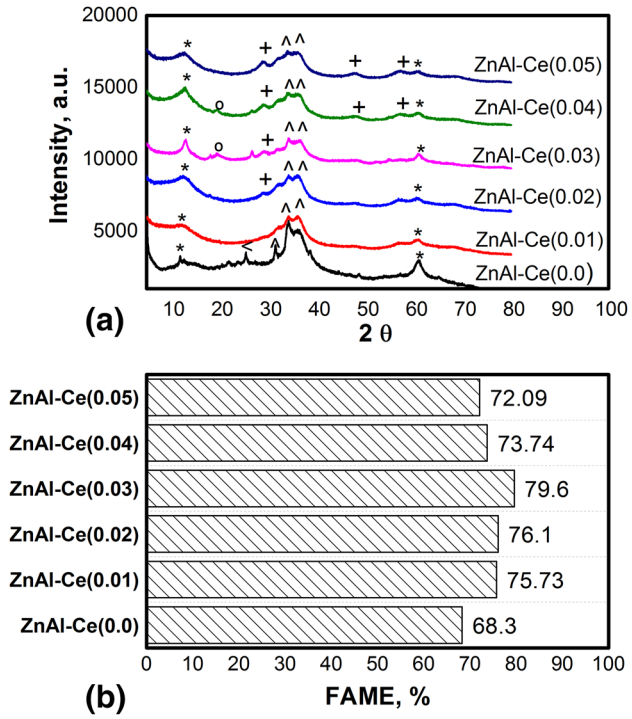

Fig. 7 **a** XRD patterns of ZnAl–Ce(X) materials activated at 200 °C. Identified species: *hydrotalcite, °hydrozincite ($Zn_5(CO_3)_2(OH)_6$), < α-alumina (Al_2O_3), +Cerium oxide (CeO_2), and ^zincite (ZnO), and **b** FAME yield of ZnAl–Ce(X) materials

Table 4 Basicity and TOF's values of ZnAl–Ce(X) materials

Catalyst	Total basicity (mmol/g)	Basic strength	TOF (s^{-1})
ZnAl–Ce(0.0)	0.1854	8.2 < pKa < 15	9.07×10^{-3}
ZnAl–Ce(0.01)	0.1990	8.2 < pKa < 15	1.04×10^{-2}
ZnAl–Ce(0.02)	0,4806	8.2 < pKa < 15	1.13×10^{-2}
ZnAl-Ce(0.03)	0.6263	8.2 < pKa < 15	1.27×10^{-2}
ZnAl–Ce(0.04)	0.5367	8.2 < pKa < 15	9.49×10^{-3}
ZnAl–Ce(0.05)	0.4893	8.2 < pKa < 15	9.11×10^{-3}
CeO_2–$Ce_2O(CO_3)_2$	0.2681	7.2 < pKa < 8.2	–

ZnAl–Ce(0.03) sample was enhanced 11.3% when compared with the ZnAl–Ce(0.0) material in the transesterification of soybean oil. This result is attributed to the larger surface area and enhanced basic properties of this material, in fact, the incorporation of Ce^{3+} reduces the temperature necessary for dehydration and dehydroxylation processes that are responsible of the total basicity observed in the ZnAl–Ce(0.03) sample.

First order reaction rate constants were estimated for ZnAl–Ce(0.0) and ZnAl–Ce(0.03) catalysts to compare the effect of cerium on the transesterification reaction rate. Assuming an irreversible reaction with excess of methanol, a pseudo first order reaction rate model with respect to triglycerides (TG) was used. Being the reaction rate equation:

$$-r_{TG} = kC_{TG} \tag{3}$$

When Eq. (3) is applied to a batch reactor, the following differential equation is obtained:

$$\left(N_{TGo}/W\right)\left(dx_{TG}/dt\right) = kC_{TGo}\left(1 - X_{TG}\right) \tag{4}$$

where N_{TGo} are the initial mol of triglycerides, W is the mass of catalyst, t is time, X_{TG} is the conversión of triglycerides, C_{TGo} is the initial concentration of triglycerides and k is the kinetic constant. The integration of Eq. (4) followed by parameter estimation through linear regression of the experimental data, lead to a value for the kinetic constant of 10.6×10^{-4} L/g_{cat}.min for the ZnAl–Ce(0.03) catalyst, which is 1.3 times higher than the material without cerium (7.8×10^{-4} L/g_{cat} min).

^{27}Al NMR spectra of ZnAl–Ce(X) samples activated at 200 °C with Ce/Al(X) = 0.01, 0.03 and 0.05 (Fig. 8) exhibit two important peaks, the first one at about 10 ppm

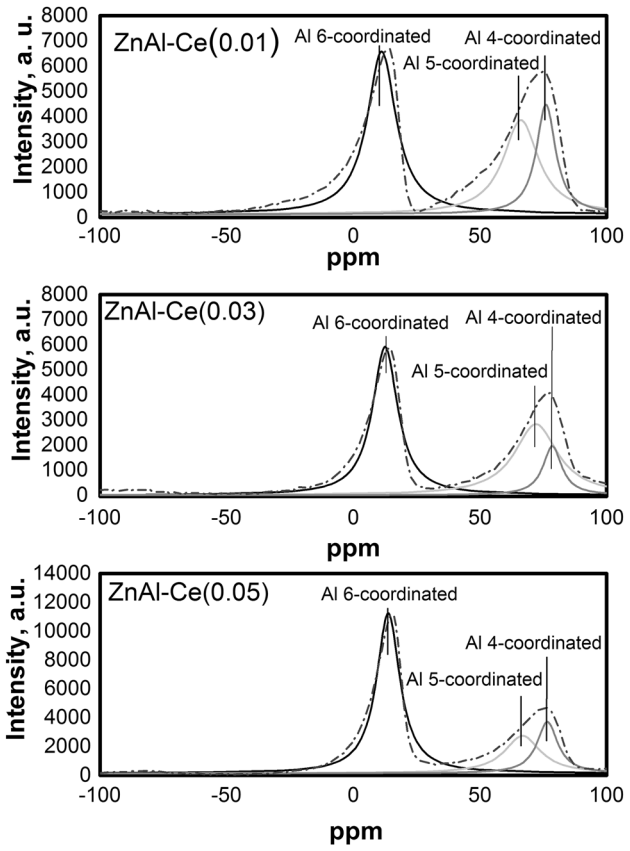

Fig. 8. ^{27}Al MAS NMR spectra of ZnAl–Ce(X) activated at 200 °C

related to aluminum species in octahedral coordination (Al 6-coordinated) and the second one at about 70 ppm, which is assigned to aluminum in tetrahedral coordination (Al 4-coordinated) [42]. This latter is not well resolved to the baseline, then, a Lorentzian deconvolution was done to distinguish the probable formation of aluminum in pentahedral (Al 5-coordinated) coordination. This distorted aluminum is assigned to oxygen defects produced during the process of dehydroxylation where some Al 6-coordinated are converted to Al 5-coordinated which generates oxygen vacancies, and then, coordinatively unsaturated sites (CUS) of aluminum, which are related to the presence of acid–basic Lewis pairs ($Al–O^-$) [42, 43].

Table 5 shows the position and relative abundance of each possible aluminum coordination in ZnAl–Ce(X) catalysts. According to the XRD and N_2 physisorption analysis, initially ZnAl–Ce(X) hydrotalcites possess aluminum in octahedral coordination; when ZnAl–Ce(X) catalysts are activated at 200 °C, dehydration and dehydroxylation processes occurred as it is shown in DTA curves (Fig. 5) resulting in a mixture of Al 6-coordinated, Al 4-coordinated, and Al 5-coordinated. Table 5 indicates that the octahedral aluminum coordination sphere easily changes into tetrahedral or pentahedral coordination when Ce is added to the brucite-like structure; obtaining a maximum in the relative population of Al 5-coordinated when the Ce/Al molar ratio is 0.03, which is more than twice the population of Al 5-coordinated present in the material without Ce. When the Ce/Al molar ratio is 0.05, the population of pentahedral aluminum suffers a significant decrease of almost half compared to ZnAl–Ce(0.03), which is attributed to the large amount of Ce that cannot be incorporated to the hydrotalcite framework. Since oxygens coordinated to Al 5-coordinated are more basic sites than that coordinated to Al 4-coordinated, this means that the high population of Al 5-coordinated could be associated with the greater activity observed for the ZnAl–Ce(0.03) catalyst, with which a FAME yield of almost 80% was obtained.

Figure 9a shows the XPS survey spectrum of ZnAl–Ce(0.03) sample when it is heated at 200°C, which indicates the emissions of Zn, Al, Ce, C and O elements. The high resolution XPS spectrum of O1s and its corresponding deconvolution (Fig. 9b) show that the chemical environment of O1s is formed by four peaks, the first one, a small band centered in a binding energy of ~ 528.4 eV which is associated with the presence of acid–basic Lewis pairs related to CeO_2. A second peak centered at ~ 530.6 eV is assigned to the presence of acid–basic Lewis pairs that belongs to ZnO. The third band at ~ 531.9 eV is attributed to Ce_2O_3 chemical bonds, and the last band at ~ 533.2 eV is related to Al_2O_3 and H_2O, which is in line with the dehydroxylation process that the brucite-like structure suffers when is heated at 200 °C, obtaining water and acid–basic Lewis pairs.

The ZnAl–Ce(0.03) material which showed the best catalytic activity was washed with acetone and without further activation reused in the transesterification of soybean oil for five subsequent reaction cycles, leading to a total decrease of 9.2% of the catalytic activity (Fig. 10). This result was attributed to the segregation of Ce as CeO_2, since Ce species tend

Table 5 Deconvolution of ^{27}Al NMR spectra of ZnAl–Ce(X) catalysts activated at 200 °C

Catalyst	Chemical shift (ppm)			Relative abundance (%)		
	Octahedral	Pentahedral	Tetrahedral	Octahedral	Pentahedral	Tetrahedral
ZnAl–Ce(0.0)	8.5	59.1	71.7	68.0	17.7	14.3
ZnAl–Ce(0.01)	11	66.2	76.1	46.5	32.7	20.8
ZnAl–Ce(0.03)	12.5	72.1	78.6	48.3	39.9	11.8
ZnAl–Ce(0.05)	13.7	67.8	76.9	60.8	22.0	17.3

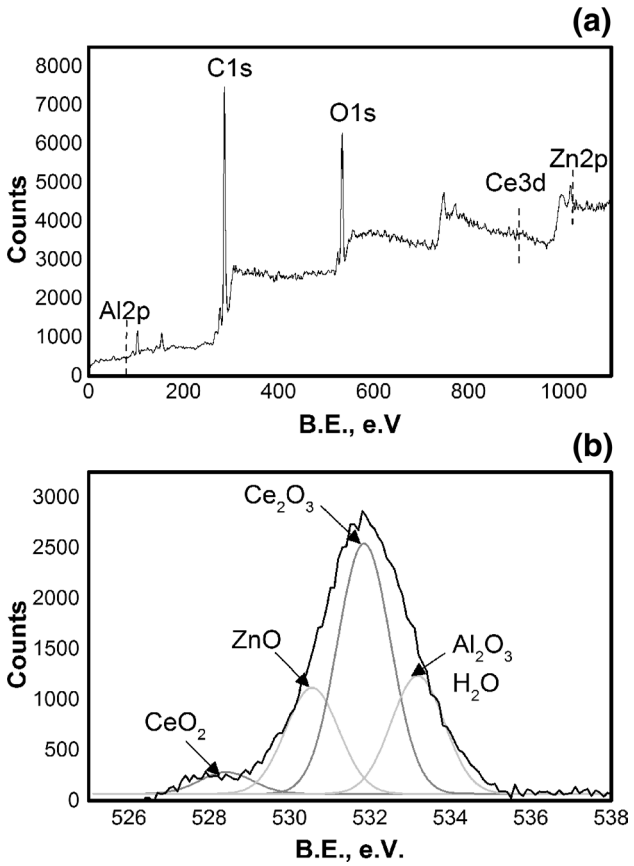

Fig. 9 **a** Survey spectra and **b** narrow spectra of O1*s* of ZnAl–Ce(0.03) catalyst activated at 200 °C

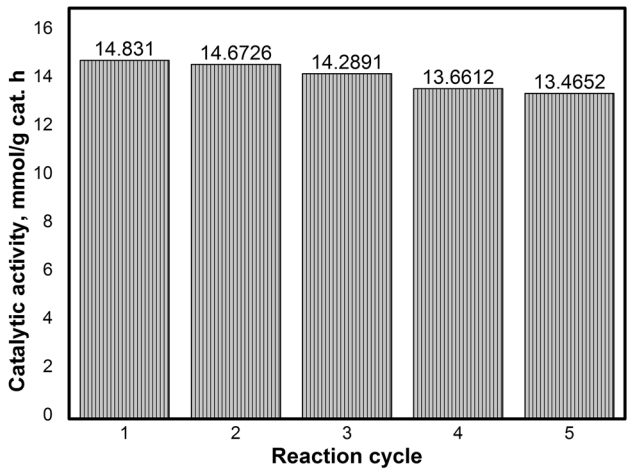

Fig. 10 Catalytic stability of ZnAl–Ce(0.03)

to achieve their most stable oxidation state. The small loss of catalytic activity of the ZnAl–Ce(0.03) catalyst in transesterification of soybean oil, demonstrated the stability of these catalysts when they are treated thermally at 200 °C. This was attributed to the formation of the active phase zincite and the partial preservation of the hydrotalcite structure, generating a high population of aluminum in pentahedral coordination.

When comparing the catalytic systems Ce/Zn/Al (this work) and Ce/Mg/Al [26] some interesting advantages associated with ZnAl–Ce(X) materials can be identified. Fist at all, the activation temperature used in this work (200 °C) was almost three times below than that used with MgAl–Ce(X) materials (575 °C). The activation temperature of the samples modulates the presence of weak, medium, and strong basic sites [15], this research stands out by the use of catalysts with weak and medium basic sites, which are enough to carry out the transesterification reaction at 200 °C with FAME yields close to 80%. Due to the low temperature of activation of ZnAl–Ce(X) materials, the hydrotalcite framework is not completely destroyed, which promotes a smaller loss of catalytic activity after five reaction cycles without further thermal activation. Whereas the high temperature of activation of MgAl–Ce(X) hydrotalcites gives rise to medium and strong basic sites that are able to carry out the transesterification reaction at 67 °C with a FAME yield of 90%. However, the reuse of MgAl–Ce(X) catalysts requires thermal reactivation at 575 °C, which causes synterization and leaching of cerium into the reaction medium, limiting thus the lifetime of MgAl–Ce(X) catalysts [26]. Hence, the ZnAl–Ce(0.03) material activated at 200 °C is a promising solid catalyst for transesterification reactions of vegetable oils with a small loss of catalytic activity.

4 Conclusion

The incorporation of cerium into the brucite-like structure of ZnAl hydrotalcite does not affect significantly the size and shape of these platy particles. However, the crystallinity of the ZnAl–Ce(X) samples is slightly affected, and a small segregation of Ce is produced as the amount of Ce incorporated is increased, resulting in catalysts with higher surface area compared to the catalyst without Ce.

The addition of cerium to ZnAl hydrotalcites decreases the temperature necessary for dehydration and dehydroxylation of the ZnAl–Ce(X) catalysts, which favors the accessibility of reactants and products to the inherent Brönsted basic sites and the formation of acid–basic Lewis pairs when these catalysts are activated at 200 °C. Indeed, when the Ce/Al molar ratio increases up to a value of 0.03, the total basicity of ZnAl–Ce(X) also augments, however, for values greater than this ratio, the total basicity begins to decrease due to the segregation of Ce as CeO_2 that was not incorporated into the hydrotalcite structure, which could be associated with the larger ionic radius of cerium.

Among the ZnAl–Ce(X) materials, the ZnAl–Ce(0.03) catalyst allowed to achieve a good balance between the loss of crystallinity, segregation of Ce and improvement of its

basic properties, resulting in a greater catalytic activity for the transesterification of soybean oil. With this catalyst it was also possible to preserve the size and shape of the platy particles of ZnAl hydrotalcite, obtaining a FAME yield of ~ 80%, which is 11.3% higher than that obtained with the catalyst without Ce. This result was attributed to its high relative population of aluminum in pentahedral coordination and thus a larger amount of acid–basic Lewis pairs. This effect was induced by the introduction of Ce in the hydrotalcite framework in both oxidation states (Ce^{3+} and Ce^{4+}) as the analysis by UV–Vis–DRS showed.

Acknowledgements Authors greatly appreciate the financial support by CIC-UMSNH. DACM thanks CONACyT for the Grant No. (487883) received during the development of this work.

References

1. Datta A, Mandal B (2016) A comprehensive review of biodiesel as an alternative fuel for compression ignition engine. Renew Sustain Energy Rev 57:799–821. https://doi.org/10.1016/j.rser.2015.12.170
2. Hassan MM, Rahman MM (2017) Performance and emission characteristics of biodiesel-diesel blend and environmental and economic impacts of biodiesel production: a review. Renew Sustain Energy Rev 74:938–948. https://doi.org/10.1016/j.rser.2017.03.045
3. Sharma YC, Singh B, Korstad J (2011) Latest developments on application of heterogeneous basic catalysts for an efficient and eco friendly synthesis of biodiesel: a review. Fuel 90:1309–1324. https://doi.org/10.1016/j.fuel.2010.10.015
4. Haziratul Mardhiah H, Chyuan Ong H, Masjuki HH, Lim S, Lee HV (2017) A review on latest developments and future prospects heterogeneous catalyst in biodiesel production from non-edible oils. Renew Sustain Energy Rev 67:1225–1236. https://doi.org/10.1016/j.rser.2016.09.036
5. Sharma YC, Singh B, Korstad J (2011) Advancements in solid acid catalysts for ecofriendly and economically viable synthesis of biodiesel. Biofuel Bioprod Biorefining 5(1):69–92. https://doi.org/10.1002/bbb.253
6. Al-Jammal N, Al-Hamamre Z, Alnaief M (2016) Manufacturing of zeolite bases catalyst from zeolite tuft for biodiesel production from waste sunflower oil. Renew Energy 93:449–459. https://doi.org/10.1016/j.renene.2016.03.018
7. Volli V, Purkait MK (2015) Selective preparation of zeolite X and A from fly ash and its use as catalyst for biodiesel production. J Hazard Mater 297:101–111. https://doi.org/10.1016/j.jhazmat.2015.04.066
8. Kouzu M, Fujimori A, Suzuki T, Koshi K, Moriyasu H (2017) Industrial feasibility of powdery CaO catalyst for production of biodiesel. Fuel Process Technol 165:94–101. https://doi.org/10.1016/j.fuproc.2017.05.014
9. Margellou A, Koutsouki A, Petrakis D, Vaimakis T, Manos G, Kontominas M, Pomonis PJ (2018) Enhanced production of biodiesel over MgO catalysts synthesized in the presence of Poly-Vinyl-Alcohol (PVA). Ind Crop Prod 114:146–153. https://doi.org/10.1016/j.indcrop.2018.01.079
10. Salinas D, Sepúlveda C, Escalona N, Gfierro JLG, Pecchi G (2018) Sol–gel La_2O_3–ZrO_2 mixed oxide catalysts for biodiesel production. J Energy Chem 27(2):565–572. https://doi.org/10.1016/j.jechem.2017.11.003
11. Lara-García HA, Romero-Ibarra IC, Pfeiffer H (2014) Hierarchical Na-doped cubic ZrO_2 synthesis by a simple hydrothermal route and its application in biodiesel production. J Solid State Chem 218:213–220. https://doi.org/10.1016/j.jssc.2014.06.040
12. Sankaranarayanan S, Antonyraj CA, Kannan S (2012) Transesterification of edible, non-edible and used cooking oils for biodiesel production using calcined layered double hydroxides as reusable base catalysts. Bioresour Technol 109:57–62. https://doi.org/10.1016/j.biortech.2012.01.022
13. Cabrera-Munguía DA, González H, Gutiérrez-Alejandre A, Rico JL, Huirache-Acuña R, Maya-Yescas R, del Río RE (2017) Heterogeneous acid conversion of a tricaprylin-palmitic acid mixture over Al-SBA-15 catalysts: reaction study for biodiesel synthesis. Catal Today 282:195–203. https://doi.org/10.1016/j.cattod.2016.10.014
14. Cabrera-Munguia DA, González H, Tzompantzi F, Gutiérrez-Alejandre A, Rico JL, Solis-Casados DA (2018) New insights on the basicity of ZnAl–Zr hydrotalcites at low temperature and their application in transesterification of soybean oil. J Mater Res 33(21):3614–3624. https://doi.org/10.1557/jmr.2018.312
15. Cavani F, Trifiró F, Vaccari A (1991) Hydrotalcite-type anionic clays: Preparation, properties and applications. Catal Today 11:173–301. https://doi.org/10.1016/0920-5861(91)80068-K
16. Sánchez-Cantú M, Pérez-Díaz LM, Maubert AM, Valente JS (2010) Dependence of chemical composition of calcined hydrotalcite-like compounds for SO_X reduction. Catal Today 150:332–339. https://doi.org/10.1016/j.cattod.2009.09.010
17. Jiang W, Lu HF, Qi T, Yan SL, Liang B (2010) Preparation, application, and optimization of Zn/Al complex oxides for biodiesel production under sub-critical conditions. Biotechnol Adv 28:620–627. https://doi.org/10.1016/j.biotechadv.2010.05.011
18. Rodrigues E, Pereira P, Martins T, Vargas F, Scheller J, Correa J, Del Nero J, Moreira SGC, Ertel-Ingrisch W, De Campos CP, Gigler A (2012) Novel rare earth (Ce and La) hydrotalcite like material: synthesis and characterization. Mater Lett 78:195–198. https://doi.org/10.1016/j.matlet.2012.03.025
19. Gao P, Li F, Zhao N, Xiao F, Wei W, Zhong L, Sun Y (2013) Influence of modifier (Mn, La, Ce, Zr and Y) on the performance of Cu/Zn/Al catalysts via hydrotalcite-like precursors for CO_2 hydrogenation to methanol. Appl Catal A 468:442–452. https://doi.org/10.1016/j.apcata.2013.09.026
20. Wang Z, Fongarland P, Lu G, Essayem N (2014) Reconstructed La, Y-, Ce modified MgAl-hydrotalcite as a solid base catalyst for aldol condensation: investigation of water tolerance. J Catal 318:108–118. https://doi.org/10.1016/j.jcat.2014.07.006
21. Genty E, Brunet J, Pequeux R, Capelle S, Siffert S, Cousin R (2016) Effect of Ce substituted hydrotalcite-derived mixed oxides on total catalytic oxidation of air pollutant. Mater Today 3(2):277–281. https://doi.org/10.1016/j.matpr.2016.01.069
22. Zhu J, Zhu Z, Zhang H, Lu H, Qiu Y, Zhu L, Küppers S (2016) Enhanced photocatalytic activity of Ce doped Zn–Al multimetal oxide composites derived from layered double hydroxides precursors. J Colloid Interface Sci 481:144–157. https://doi.org/10.1016/j.jcis.2016.07.051
23. Xu M, Pan G, Meng Y, Guo Y, Wu T, Chen H (2019) Effect of Ce^{3+} on the photocatalytic activity of MAlCe ternary hydrotalcites-like compounds in methylene blue photodegradation. Appl Clay Sci 170:46–56. https://doi.org/10.1016/j.clay.2019.01.011
24. Saikia P, Miah AT, Malakar M, Bordoloi A (2015) Enhanced catalytic activity of supported gold catalysts for oxidation of noxius environmental pollutant CO. Indian J Mater Sci 2015:1–10. https://doi.org/10.1155/2015/658346

25. Yang S-Q, He J-P, Zhang N, Sui X-W, Zhang L, Yang Z-X (2018) Effect of rare-earth element modification on the performance of Cu/ZnAl catalysts derived from hydrotalcite precursor in methanol steam reforming. J Fuel Chem Technol 46(2):179–188. https://doi.org/10.1016/S1872-5813(18)30010-0
26. Soares Días AP, Bernardo J, Felizardo P, Neiva Correia MJ (2012) Biodiesel production over thermal activated cerium modified Mg-Al hydrotalcites. Energy 41:344–353. https://doi.org/10.1016/j.energy.2012.03.005
27. Zhang D, Zhang X, Li Y, Wang S, Wang X, Jiang Z (2018) Incorporation of Ce^{3+} ions into dodecatungstophosphoric acid for the production of biodiesel from waste cooking oil. Mater Sci Eng C 92:931–992. https://doi.org/10.1016/j.msec.2018.07.047
28. Ambat I, Srivastava V, Haapaniemi E, Sillanpää M (2019) Nanomagnetic potasium impregnated ceria as catalyst for the biodiesel production. Renew Energy 139:1428–1436. https://doi.org/10.1016/j.renene.2019.03.042
29. Thitsartarn W, Maneerung T, Kawi S (2015) Highly active and durable Ca-doped Ce-SBA-15 catalyst for biodiesel production. Energy 89:946–956. https://doi.org/10.1016/j.energy.2015.06.039
30. Yan B, Zhang Y, Chen G, Shan R, Ma W, Liu C (2016) The utilization of hydroxyapatite supported CaO-CeO_2 catalyst for biodiesel production. Energy Convers Manage 130:156–164. https://doi.org/10.1016/j.enconman.2016.10.052
31. Fraile JM, García N, Mayoral JA, Pires E, Roldán L (2010) The basicity of mixed oxides and the influence of alkaline metals: the case of transesterification reactions. Appl Catal A 387(1–2):67–74. https://doi.org/10.1016/j.apcata.2009.05.031
32. Rostam JM, Boudart M (1982) Experimental criterion for the absence of artifacts in the measurement of rates of heterogeneous catalytic reactions. Ind Eng Chem Fundam 21:438–447. https://doi.org/10.1021/i100008a022
33. Turianicova E, Kañuchova M, Zorkovská A, Holub M, Bujnakova Z, Dutková E, Baláž M, Findoráková L, Balintová M, Obut A (2016) CO2 utilization for fast preparation of nanocrystalline hydrozincite. J CO Util 16:328–335. https://doi.org/10.1016/j.jcou.2016.08.007
34. Liu H, Le Q (2016) Synthesis and performance of cerium oxide as anode materials for lithium ion batteries by a chemical precipitation method. J Alloy Compd 669:1–7. https://doi.org/10.1016/j.jallcom.2016.01.235
35. Seftel EM, Popovici E, Mertens M, De Witte K, Van Tendeloo G, Cool P, Vansant EF (2008) Zn-Al layered double hydroxides: synthesis, characterization and photocatalytic application. Microporous Mesoporous Mater 113:296–304. https://doi.org/10.1016/j.micromeso.2007.11.029
36. Koilraj P, Kannan S (2010) Phosphate uptake behavior of ZnAlZr ternary layered double hydroxides through surface precipitation. J Colloid Interface Sci 341:289–297. https://doi.org/10.1016/j.jcis.2009.09.059
37. Velu S, Sabde DP, Shah N, Sivasanker S (1998) New hydrotalcite-like anionic clays containing Zr^{4+} in the layers: Synthesis and physicochemical properties. Chem Mater 10:3451–3458
38. Della Mea GB, Matte LP, Thill AS, Lobato FO, Benvenutti EV, Arenas LT, Jürguensen A, Hergenröder R, Poletto F, Bernardi F (2017) Tuning the oxygen vacancy population of cerium oxide ($CeO_{2-x,}$ 0 %3c x %3c 0.5) nanoparticles. Appl Surf Sci 422:1102–1112. https://doi.org/10.1016/j.apsusc.2017.06.101
39. López T, Ramos E, Bosch P, Asomoza M, Gómez R (1997) DTA and TGA characterization of sol–gel hydrotalcites. Mater Lett 30:279–282. https://doi.org/10.1016/S0167-577X(96)00214-5
40. Hegel P, Andreatta A, Pereda S, Bottini S, Brignole EA (2008) High pressure phase equilibria of supercritical alcohols with triglycerides, fatty esters and cosolvents. Fluid Phase Equilibr 266:31–37. https://doi.org/10.1016/j.fluid.2008.01.016
41. Sanna R, Medas D, Poddda F, Meneghini C, Casu M, Lattanzi P, Scorciapino MA, Floris C, Cannas C, de Giudici G (2015) Binding of bis-(2-ethylhexyl) phthalate at the surface of hydrozincite nanocrystals: an example of organic molecules absorption onto nanocrystalline minerals. J Colloid Interface Sci 457:298–306. https://doi.org/10.1016/j.jcis.2015.07.016
42. Álvarez MG, Chimentão RJ, Barrabés N, Föttinger K, Gispert-Guirado F, Kleymenov E, Tichit D, Medina F (2013) Structure evolution of layered double hydroxides by ultrasound induced reconstruction. Appl Clay Sci 83–84:1–11. https://doi.org/10.1016/j.clay.2013.08.006
43. Coster D, Fripiat JJ (1993) Memory effects in gel-solid transformations: coordinately unsaturated Al sites in nanosized aluminas. Chem Mater 5:1204–1210. https://doi.org/10.1021/cm00033a004

Affiliations

Denis A. Cabrera-Munguia[1] · Horacio González[2] · Mónica Barreto-Gutiérrez[2] · Aída Gutiérrez-Alejandre[3] · José L. Rico[2] · Dora A. Solís-Casados[4]

[1] Facultad de Ciencias Químicas, Universidad Autónoma de Coahuila, 25280 Saltillo, Coahuila, Mexico

[2] Facultad de Ingeniería Química, Universidad Michoacana de San Nicolás de Hidalgo, 58030 Morelia, Michoacán, Mexico

[3] UNICAT, Depto. De Ingeniería Química, Facultad de Química, Universidad Nacional Autónoma de México, 04510 Mexico City, Mexico

[4] Centro Conjunto de Investigación en Química Sustentable, UAEM-UNAM, 50200 Toluca, Mexico